

FABRICATION OF VISIBLE LIGHT PHOTODETECTOR USING CO-EVAPORATED Cu_2SnS_3 THIN FILMS

T. S. REDDY^a, M. C. SANTHOSH KUMAR^{b,*}

^aDepartment of Physics, P.B Siddhartha College of Arts and Science, Vijayawada, Andhra Pradesh, India 520010

^bNational Institute of Technology, Tiruchirappalli, Tamil Nadu, India 620015

We adopt co-evaporation method for the deposition of copper tin sulfide (Cu_2SnS_3) thin films at a constant substrate temperature of 250 °C. The film thickness was varied in the range of 285-910 nm. The physical properties of Cu_2SnS_3 films were studied using appropriate characterization techniques. The XRD analysis reveals the tetragonal crystal structure of Cu_2SnS_3 films. The SEM images show the granular shaped crystallites distributed entire surface of the films. The energy band gap of the films are in the range of 1.73 -1.10 eV. Significant improvements in electrical properties are observed for the p-type conducting CTS films with thickness. The reduction in band gap to near optimum value along with the improved electrical properties enhances the prospects of Cu_2SnS_3 as a prospective absorber layer for solar cells. Photodetectors have been fabricated using the sample of thickness 496 nm. The photoresponse parameters such as photoconductivity (σ), sensitivity(s), specific detectivity (D), External Quantum Efficiency (EQE) and responsivity (R) were calculated for the device of glass/CTS/Ag from the I-V measurement under the illumination of 100 mW/cm² white light source.

(Received August 20, 2019; Accepted November 11, 2019)

Keywords: Cu_2SnS_3 thin films, Structural properties, Electrical properties, Band gap, Co- evaporation

1. Introduction

During the last decades, silicon solar cell technology is the most important dynamic force, which is expensive because of the requirement of high purity silicon (> 99.9999) and consequent high wafer costs. Hence, novel materials are required to fabricate low cost and non-toxic solar cells. The thin film solar cell technology is one of the best alternatives to reduce the modules cost because it offers significant advantages, both in terms of material and fabrication, as compared to the silicon-based technology.

In recent years, Cu-Sn-S ternary compounds have reached great interest for optoelectronic applications. These ternary systems exhibited different stable phases [1]. Cu_2SnS_3 (CTS) is a prospective absorber layer for the fabrication of solar cells due to the high stability, favorable optical and electrical properties. Normally, CTS exhibits cubic structure [2] at the high temperature (>750 °C) while the low temperature (<750 °C) phases of CTS are tetragonal [3], monoclinic [4] and triclinic [5]. CTS compound semiconductor belongs to the I-IV-VI family, which is attracted much attention for solar cells, photodiodes and sensors.

It is a capable absorber layer for solar cell applications due to the p-type direct band gap (0.9-1.5 eV) and higher absorption coefficient (>10⁴ cm⁻¹). Moreover, the elements (Cu, Zn, Sn, and S) are abundance in earth crust, non-toxic and inexpensive. Formerly, Cu_2SnS_3 thin films were deposited in various physical and chemical techniques namely co-evaporation [6, 7], sputtering [8-10], electron beam evaporation [11, 12] and pulsed laser deposition [13], spin coating [3, 14], spray pyrolysis [5-17], solvothermal synthesis [18, 19] and Successive ionic Layer Adsorption and Reaction (SILAR) [20-22].

* Corresponding author: santhoshmc@nitt.edu

The physical properties of Cu_2SnS_3 thin films as a function of substrate temperature was reported elsewhere [23]. These results conclude that the film deposited at 250°C shows better optical and electrical properties compared to other substrate temperatures. Hence, these investigations are extended by keeping the substrate temperature constant and varying the film thickness. In the present work, co-evaporation technique is employed to deposit the Cu_2SnS_3 thin films on glass substrates at various thicknesses 285-910 nm at a constant substrate temperature of 250°C . Similar studies are available for chemically deposited Cu_2SnS_3 [24, 25]. The variation in structural, optical, morphological and electrical properties were investigated and reported here. The photodetector parameters like photosensitivity, responsivity and specific detectivity of the CTS visible light photodetector are reported for the first time using co-evaporation technique.

2. Experimental

Co-evaporation technique has been employed to deposit copper tin sulfide (Cu_2SnS_3) thin films on ultrasonically cleaned glass substrates at a temperature of 250°C with various thickness 285-910 nm. The ultrasonically cleaned glass substrates are used to deposition of CTS thin films and the cleaning procedure used here is reported elsewhere [23]. The experimental conditions for the deposition of different thickness of Cu_2SnS_3 thin films are found elsewhere [23]. The structural studies of the co-evaporated Cu_2SnS_3 thin films were investigated by Rigaku ultima XRD and Micro-Raman spectroscopy (Horiba labRAM HR). The surface topology and elemental composition of the films were examined using Zeiss Ultra 55 FESEM attached with Oxford EDS system. The morphology of the films recorded using AFM at room temperature. The optical absorbance of the deposited films was recorded using the JASCO V-670 UV-Vis-NIR spectrometer. Hall effect measurement in vander pauw configuration (ECOPIA HMS-5000) was used to study the electrical properties of the films. The photo response of the films are recorded at room temperature by two probe method using Keithley (6517A) under Oriel solar simulator (AM 1.5 G) spectrum of illumination intensity 100 mW/cm^2 at a constant applied bias 5V.

3. Results and discussion

3.1 Structural analysis

Fig.1 shows the X-ray diffraction spectra of Cu_2SnS_3 thin films deposited with different thicknesses. The presence of peaks at $2\theta = 28.46^\circ, 38.26^\circ, 44.52^\circ, 47.45^\circ, 64.78^\circ, 67.70^\circ$ and 77.89° are belong to the Cu_2SnS_3 with tetragonal phase (JCPDS 89-4714). XRD spectra show that the deposited films exhibit polycrystalline nature and the peaks can be assigned to the (112), (211), (213), (204), (314) (323) and (413) planes respectively. All the films show (112) plane as the preferred orientation. A similar result reported by Fernandes et al. [2] and Reddy et al. [23]. As the film thicknesses increased to 910 nm, the diffraction peak (112) become more intense, which indicates an enhancement in the crystallinity of the films. Apart from Cu_2SnS_3 phase, additional phases corresponding to Cu_2S (JCPDS- 29-0578) and Sn_2S_3 (JCPDS 75-21830) (indicated by ∇ and \bullet) are observed for the film thickness above 496 nm. Similar results of Cu_2SnS_3 thin films were reported by Fernandes et al. [2], Shelke et al. [25] and Chalapathi et al. [26]. In XRD spectra observed that a marginal shift in the position of the peaks, which is due to the existence of strain between the amorphous substrate and the films.

The lattice parameters of the tetragonal crystal structure can be evaluated by the relation

$$\frac{1}{d_{(hkl)}^2} = \left[\frac{h^2 + k^2}{a^2} \right] + \frac{l^2}{c^2} \quad (1)$$

where d is the spacing between the layers and (h, k, l) are the miller indices. Table 1 shows the lattice parameter values of CTS thin films. These are good agreement with the Cu_2SnS_3 phase (JCPDS 89-4714). The marginal variation in the lattice parameters might be due to the existence of

strain in the films. The structural parameters of the layers were calculated from the XRD data using the following equations

$$\text{average crystallite size (D)} = \frac{0.94\lambda}{\beta \cos\theta} \quad (2)$$

$$\text{micro strain}(\epsilon) = \frac{\beta \cos\theta}{4} \quad (3)$$

$$\text{dislocation density } (\delta) = \frac{15\epsilon}{aD} \quad (4)$$

The calculated values are tabulated in Table 2. The average crystallite size increased from 6 nm to 14 nm, while micro strain and dislocation density decreased with increase of film thickness from 285 nm to 910 nm. Manjulavalli et al. [24] also reported similar structural properties for the chemical bath deposited Cu_2SnS_3 thin films.

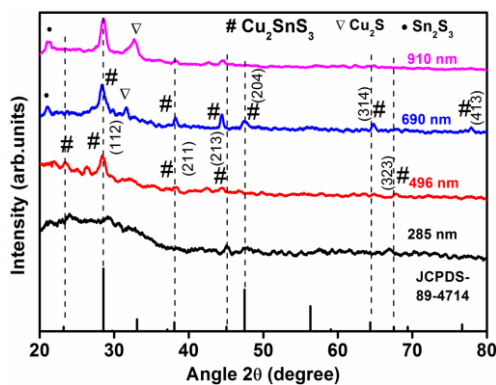


Fig. 1. XRD patterns of Cu_2SnS_3 thin films with various thickness.

Table 1. Lattice parameters of Cu_2SnS_3 films with different film thickness.

Thickness (nm)	Lattice parameters	
	a (Å)	c (Å)
JCPDS (89-4714)	5.413	10.824
285	5.494	10.888
496	5.423	10.860
690	5.412	10.860
910	5.403	10.835

Table 2. Structural parameters of Cu_2SnS_3 thin films deposited different thickness.

Thickness (nm)	FWHM (β) (radians)	Average Crystallite size (D) (nm)	Micro strain (ϵ)	Dislocation density (δ) $\times 10^{17}(\text{m}^{-2})$
285	1.29	6	0.31	14.10
496	1.18	7	0.28	11.06
690	0.73	12	0.17	3.926
910	0.60	14	0.14	2.776

3.2. Raman Spectroscopy

The Raman spectra of Cu_2SnS_3 films deposited at various film thickness shown in Fig. 2. It contains the various Raman bands at 62 cm^{-1} , 71 cm^{-1} , 127 cm^{-1} , 285 cm^{-1} , 332 cm^{-1} and 472 cm^{-1} . The characteristics Raman modes of CTS films are observed at 285 cm^{-1} and 332 cm^{-1} for the film 496 nm . The films deposited above 496 nm exhibits tetragonal phase Cu_2SnS_3 along with binary phases Cu_2S and Sn_2S_3 are observed. Thus Raman studies strongly support with XRD analysis. Reports suggest that the observed Raman band at 332 cm^{-1} corresponds to the tetragonal structure of Cu_2SnS_3 layers [20, 23]. The Raman mode at 285 cm^{-1} is one of the characteristic Raman peak of Cu_2SnS_3 thin films. A similar Raman band was reported by Han et al. [5]. The mode at 472 cm^{-1} belongs to the Cu_2S [27]. The observed Raman band at 62 cm^{-1} [28] and 71 cm^{-1} is assigned to the Sn_2S_3 binary phase [29]. The observed low intensity 127 cm^{-1} Raman mode belongs to the SnS binary phase [30].

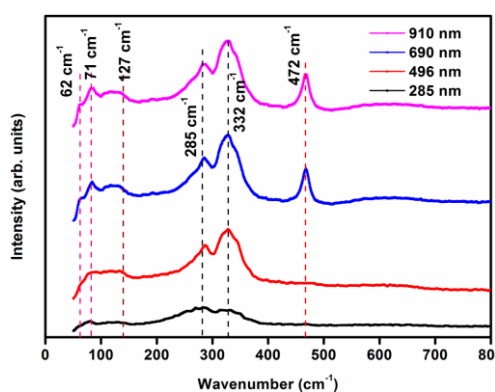


Fig. 2. Raman spectra of Cu_2SnS_3 thin films at different thicknesses.

3.3. Elemental analysis

The presence of Cu, Sn and S are confirmed by EDX measurement in all the deposited films. The atomic percentage of the elements is reported in Table 3. The ratio of Cu/Sn increased from 1.16 to 2.09 with increase of film thickness. It is clear from the Table 3 the supply of sulfur quantity ($\text{S}/\text{Cu}+\text{Sn} \approx 1$) is sufficient for the formation of Cu_2SnS_3 films. From the compositional analysis it is noticed that the Sn content in the films decreased with thickness. The film deposited at higher thickness (910 nm) have near stoichiometric ratio of $\text{Cu}/\text{Sn} = 2.09$, which is due to the Cu_2SnS_3 phase have the faster reaction rate than the high vapor pressure rates of Cu_2S and Sn_2S_3 . Zhang et al. [31] also reported a similar tendency in Cu/Sn ratio of Cu_2SnS_3 thin films.

Table 3. Atomic percentage of Cu, Sn and S in at different thickness of Cu_2SnS_3 thin films.

Thickness (nm)	Composition results (at. %)			Ratio Cu/Sn	Ratio S/Cu+Sn
	Cu	Sn	S		
285	25.76	22.15	50.16	1.16	1.04
496	29.63	19.30	51.06	1.53	1.06
690	32.02	16.56	51.37	1.93	1.05
910	34.35	16.40	52.25	2.09	1.02

3.4 SEM and AFM analysis

The FESEM micrographs of all films are shown in Fig. 3 (a)-(d). From the figures, it is observed that densely packed granular shaped crystallites are homogeneously distributed across the substrate. These micrographs showed the dependence of morphology on the film thickness.

From the Fig. 3 (a-d) clearly noticed that the distribution of granular shaped crystallites are continued without any voids across the film.

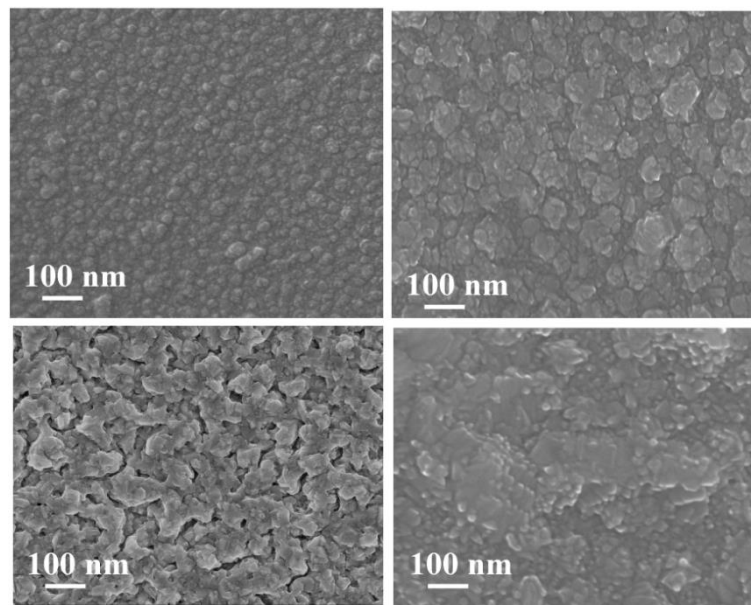


Fig. 3. SEM micrographs (a) 285 nm (b) 496 nm (c) 690 nm and (d) 910 nm of the Cu_2SnS_3 thin films.

From the pictures clearly observed that a significant change in the crystallites size of the deposited films with thickness. The granular shaped crystallites with spherical shape across the substrate surface are observed for the film deposited at lower thickness. For the films deposited at higher thickness, these granular shaped crystallites are transformed in to bigger crystallites with regular shape. The film deposited at higher thickness consists of more compact and adherent granular shaped crystallites. The cross-sectional view of all the samples deposited on the soda-lime glass substrate at a constant substrate temperature of 250 °C is shown in Fig. 4 (a)-(d).

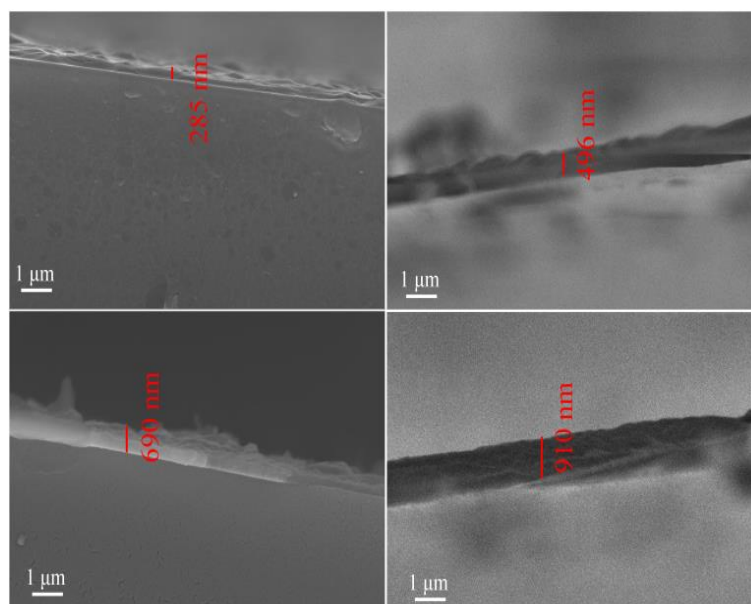


Fig. 4. The cross sectional view (a) 285 nm (b) 496 nm (c) 690 nm and (d) 910 nm of the Cu_2SnS_3 thin films.

Fig.5. (a)-(d) depicts the AFM 3D images of Cu_2SnS_3 thin films deposited at different thicknesses. The AFM images are scanned for an area of $5\mu\text{m} \times 5\mu\text{m}$. From these micrographs, noticed that Cu_2SnS_3 films are free from voids. The grain size (140 - 291 nm) and surface roughness (10-38 nm) of the deposited films increased with increase of film thickness from 285 nm to 910 nm. Chihi et al. [32] have observed increase of roughness for electro-deposited Cu_2SnSe_3 thin films. A similar trend in the surface of the films with thickness reported for Sn_2S_3 [28], In_2S_3 [33] and In_2O_3 [34] thin films. The variation in the RMS values of the deposited films due to the variation in the distribution of the grains on the films.

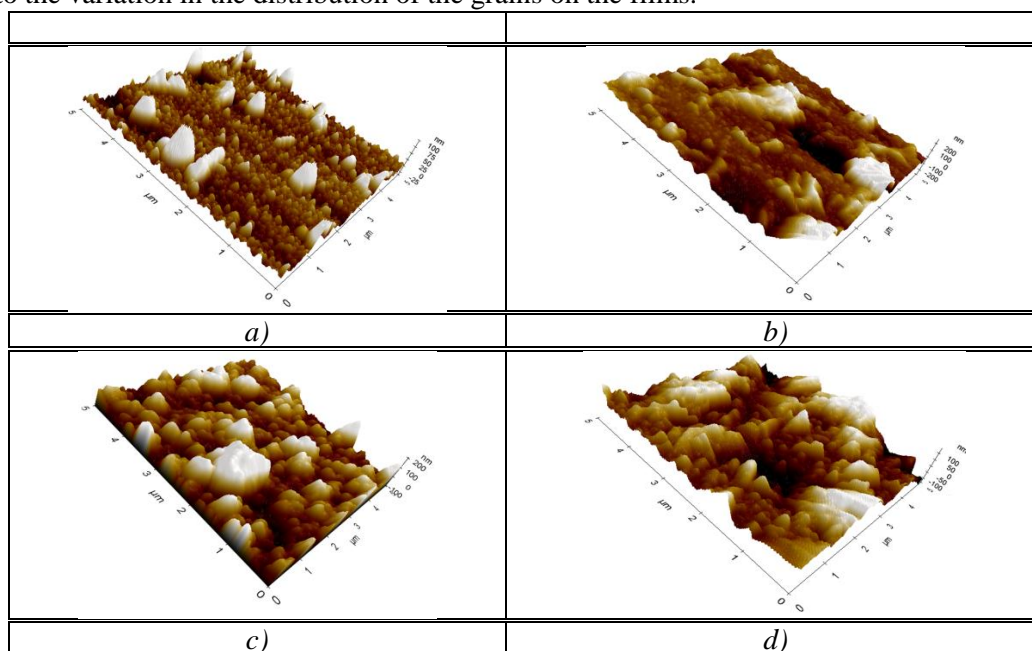


Fig. 5. AFM micrographs of SnS thin films grown at (a) 285 nm (b) 496 nm (c) 690 nm and (d) 910 nm.

3.5. Optical properties

Fig.6 shows the optical absorption of the films deposited at thickness, 285, 496, 690 and 910 nm. A sharp fall in absorption was noticed at the fundamental absorption edge or critical wave length (λ_c) for all films. The critical wave length position of the deposited films shifts from lower wave length to higher wave length region with increase of film thickness. Such a shift at the absorption edge was observed in Cu_2SnS_3 [24], Cu_4SnS_4 [35], SnS [36], ZnS [37] thin films. It indicates that the absorbance of visible light is improved with film thickness. Therefore, the deposited films are emerging material as an absorber layer for solar cells. The shift in the absorption edge towards higher wave length indicates the reduction of the energy band gap (E_g) of the films.

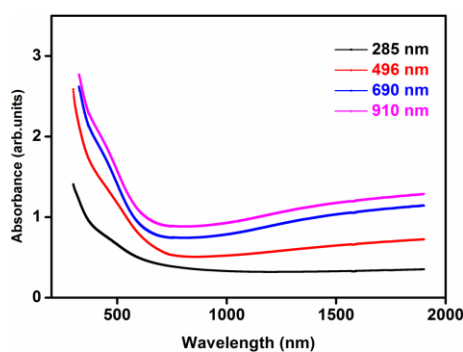


Fig. 6. Absorbance spectra of the Cu_2SnS_3 films deposited at different thickness.

The optical band gap (E_g) was evaluated using the standard equation

$$\alpha h\nu = M(h\nu - E_g)^{1/2} \quad (5)$$

where E_g is the optical band gap, α is absorption coefficient, M is a constant. The Fig. 7 (a)-(d) shows the Tauc plot between $(\alpha h\nu)^2$ vs $h\nu$ of the deposited films. The band gap values are determined from the intersect of straight line of the plot of $(\alpha h\nu)^2$ vs $h\nu$. The deposited films show that the absorption coefficient (α) is greater than 10^5 cm^{-1} at the absorption edge region. From the Fig. 7 (a)-(d) observed that the decrease in energy band gap from 1.73-1.10 eV with increase of film thickness. A similar continuous trend in band gap was observed for Cu_2SnS_3 [24, 25], Cu_4SnS_4 [35], ZnS [37] and In_2S_3 [33, 38]. The variation in the band gap may be broadly affected by many factors such as crystallite size, chemical compositional, crystal structure, defects and residual strain. In the present investigation the decrease of band gap can be correlated to the average crystallite size and composition of the layers.

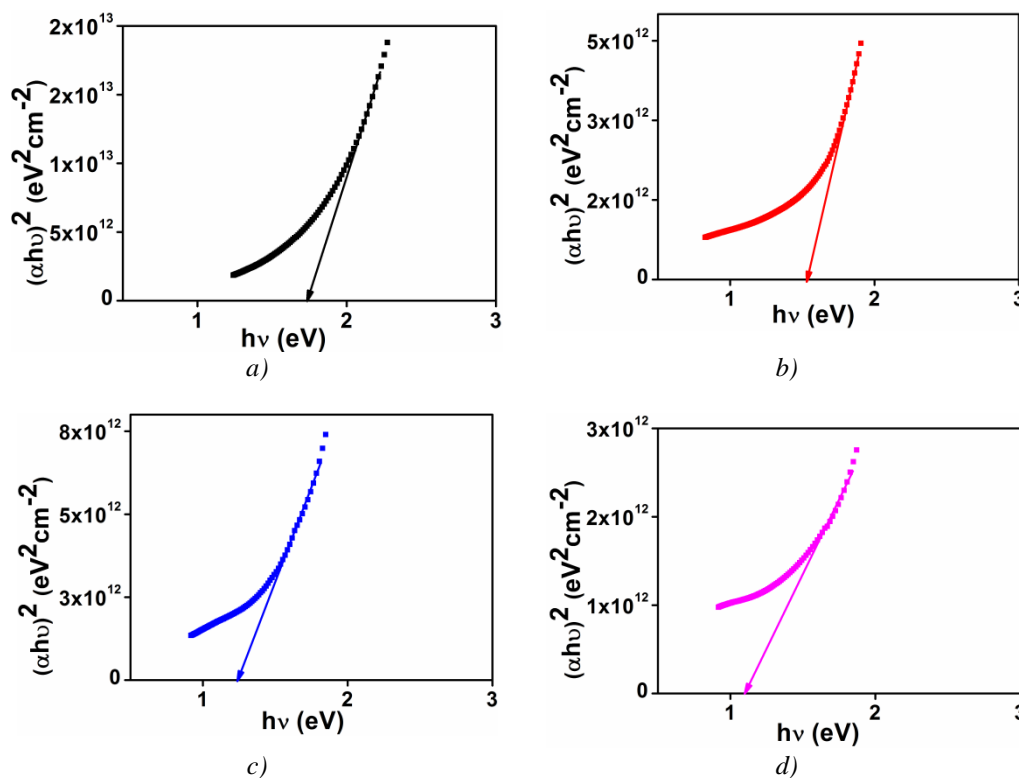


Fig.7. Plot of $(\alpha h\nu)^2$ Vs $(h\nu)$ of Cu_2SnS_3 thin films of thickness (a) 285 nm (b) 496 nm (c) 690 nm and (d) 910 nm.

The variation in the band gap of the deposited films with average crystallite size is describe by the quantitative form [39, 40]

$$E_g^{(\text{nano})} = E_g^{(\text{bulk})} + \frac{\hbar^2 \pi^2}{2\mu r^2} \quad (6)$$

where r is the particle radius, μ is the effective mass. Fig. 8 shows the band gap variation as a function of thickness and average crystallite size of the films. In Fig. 8, the black continues line represents the average crystallite size, blue continues line represents the band gap calculated from the relation (6) and the red color filled circles are experimental band gap. It is noticed that the experimental band gap values are follows the relation (6). The solid line curve (blue) of fig.8

nearly fits to our experimental data points. From the figure, it can be noticed that the dependence of band gap on the thickness and average crystallite size. Benedetto et al. [41] also reported a similar trend in the energy band gap of the electrodeposited CTS thin films. In addition to that, the elemental ratio of Cu/Sn of the films increases from 1.16 to 2.09 with increase of film thickness (285-910 nm). In the present study, the formation of binary phases (Cu_2S and Sn_2S_3) might be due to the deviation in the Cu/Sn ratio of the deposited layers, which is supported by XRD and Raman analysis. The reported direct band gap values of tetragonal Cu_2SnS_3 are in the range of 1.10-1.35 eV [7] and 0.96 eV [2] for Cu_2SnS_3 cubic structure. The band gap values of the deposited films decrease from 1.73-1.10 eV with increase of Cu/Sn ratio (1.16 to 2.09). At higher thickness of the film (Cu/Sn =2.09) shows a stoichiometric ratio with a lower band gap value of 1.10 eV, which is closer to the reported band gap value of tetragonal Cu_2SnS_3 . When the Cu/Sn is 1.16, the film (285 nm) shows a higher band gap (1.73 eV). The minute deviation from the reported band gap values at the lower thickness (285 nm) and lower Cu/Sn ratio (1.16) is due to the deviation from stoichiometry or film inhomogeneity. Recently Shelke et al. [25] also reported a similar trend in energy band gap of Cu_2SnS_3 thin films (1.36 to 0.98 eV) as a function of thickness (526-1000 nm). Robles et al. [6] reported the variation in band gap (0.9-1.25 eV) with increase of Cu/Sn ratio (0.5 to 2.8) of co-evaporated CTS thin films. Chalapathi et al. [26] reported a similar behavior in the band gap of co-evaporated Cu_2SnS_3 films. Hence, in the present study noticed that the reduction in the band gap is due to the variations in the average crystallite size and composition.

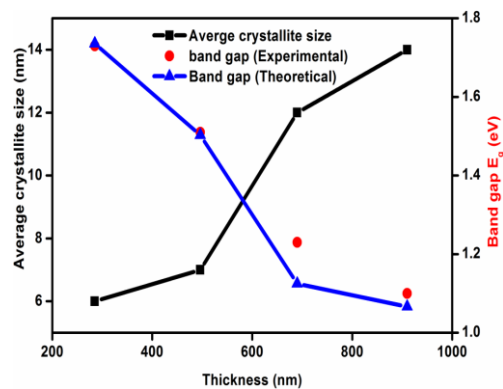


Fig. 8. Band gap variation and average crystallite size with thickness of the deposited films.

3.6. Electrical studies

Hall Effect via Van der Pauw technique is adopted to study the electrical properties of the Cu_2SnS_3 thin films at room temperature. P-type behavior has been observed for all the deposited films. A similar nature of CTS was observed by other researchers as well [13, 25, 26]. The electrical properties of the films were listed in Table 4. It is clear that the resistivity of the films decreased from $1.76 \times 10^{-2} \Omega \text{ cm}$ to $1.02 \times 10^{-3} \Omega \text{ cm}$ with increase of film thickness. These values are lower than the values reported by Chalapathi et al [26]. Earlier reported a similar variation in resistivity for CTS thin films [6, 13, 26]. In the present investigation the electrical properties of the deposited layer are influenced by the chemical composition. The resistivity of the deposited films mainly depends on the Cu/Sn ratio of the deposited films. In the present study, the reduction in resistivity (10^{-2} - $10^{-3} \Omega \text{ cm}$) of the films might be due to the increase of Cu/Sn ratio (1.16 to 2.09). The dependence of resistivity values on the Cu/Sn ratio of co-evaporated Cu_2SnS_3 thin films was reported earlier [6, 10, 13]. From the EDX analysis, it is noticed that the copper content is increases with increase of film thickness. In summary, the decrease in the resistivity can be correlated to the occurrence of higher copper content in the films.

Table 4. Electrical properties of the Cu_2SnS_3 thin films deposited at different thickness.

Thickness (nm)	Carrier concentration n_o (cm^{-3})	Resistivity (Ω cm)	Mobility $\text{cm}^2\text{V}^{-1}\text{S}^{-1}$	Carrier type
285	2.39×10^{20}	1.76×10^{-2}	1.48	P
496	1.56×10^{21}	2.58×10^{-3}	1.55	P
690	2.81×10^{21}	1.31×10^{-3}	1.70	p
900	2.85×10^{21}	1.02×10^{-3}	2.11	P

3.7 Photoconductivity

Fig. 9 (a) shows the schematic representation of the photodetector with Ag as Ohmic contacts. The I-V measurement for the photodetector is performed using two probe method under white light (AM 1.5 G spectrum). The photocurrent of the photodetector recorded at ON/OFF switch cycle of 20 s at 5V bias voltage. In the present study, the photoconductivity of the film is calculated using the equation

$$\sigma = \frac{Id}{VA} \quad (7)$$

where I is the measured current, V is the bias voltage, d is the film thickness (496 nm), and A is the device area (0.06 cm^2). A positive photocurrent response has been observed. A similar photo response has been observed in several materials [42, 43, 44]. Figure 9 (b) shows that the photoconductivity versus time of the photodetector. During illumination (light on), photocurrent increases continuously with time while during the dark (light off), a sudden fall in the photocurrent followed by a slow decay. From the figure, it is observed that the reversibility and stability of the photodetector. It is noticed that the ratio of electrical conductivity under light to the electrical conductivity under dark (σ_L / σ_D) is about 1.13. The photosensitivity of the detector is the ratio of the photoconductivity to the dark conductivity given by the equation

$$\text{Photosensitivity} = \frac{\sigma_\lambda}{\sigma_D} \quad (8)$$

where σ_λ photoconductivity given by $\sigma_\lambda = \sigma_L - \sigma_D$. In the present work, Responsivity (R) and specific dectivity (D) was reported using 100 mW/cm^2 light source and the effective area (0.06 cm^2). Generally, the Responsivity (R) is the ratio of photocurrent per unit area to the unit illumination intensity of light source. The responsivity (R) of the photodetector can be calculated using the equation [42, 45]

$$R = \frac{I_\lambda}{L_\lambda S} \quad (9)$$

where I_λ is the photocurrent ($I_\lambda = I_{\text{light}} - I_{\text{dark}}$), L_λ is the incident light source intensity (100 mW/cm^2) and S is the lighting area. The External Quantum Efficiency (EQE) of the deposited films calculated the following formula [46]

$$EQE = \frac{Rhc}{\lambda_{\text{incident}}} \times 100 \quad (10)$$

where R is Responsivity and λ is the wave length of the halogen source (the average wavelength of the visible region is 532 nm). The EQE of the fabricated photodiodes is calculated as $0.33 \times 10^2 \%$. A similar result reported by Dias et al. [45] for the solution based Cu_2SnS_3 thin film photodetector.

The specific detectivity (D) is the capability of the device to sense the least radiant signal and calculated using the following equation [46]

$$D = \frac{R}{(2 q J_{\text{dark}})^{1/2}} \tag{11}$$

The calculated optical parameters of the device are $R=0.14 \text{ AW}^{-1}$ and $D=24 \times 10^6 \text{ Jones}$. Similar values have been reported for other material devices [44,47]. The Fig. 10 shows the variation in photoconductivity as a function of time. From the figure, it is observed that the light source is OFF condition the photocurrent decreases rapidly after that it reaches starting position through slow decay. At the light source is cut off position the device exhibit transient current due to the presence of the trap states in the films. The rapid decay (fast decay) arises due to the direct recombination between the charge carrier pairs. The fast decay can be calculated by the relation

$$I(t) = I_{\text{dark}} \exp \left(-\tau / \tau_s \right) \tag{12}$$

where τ_s is the surface carrier life time and I_{dark} is the dark current at the source was switched on and off. The slow decay time was calculated by the equation

$$I(t) = I_{\text{dark}} \exp \left(-\tau / \tau_b \right) \tag{13}$$

where τ_b is the bulk carrier life time. The evaluated fast decay and slow decay time was 0.5 second and 1.52 second. It is clear that the time taken for slow decay is higher than the fast decay. The observed time delay in slow decay could be due the existence of trapping states. Similar results are also reported for other materials [48,49] .

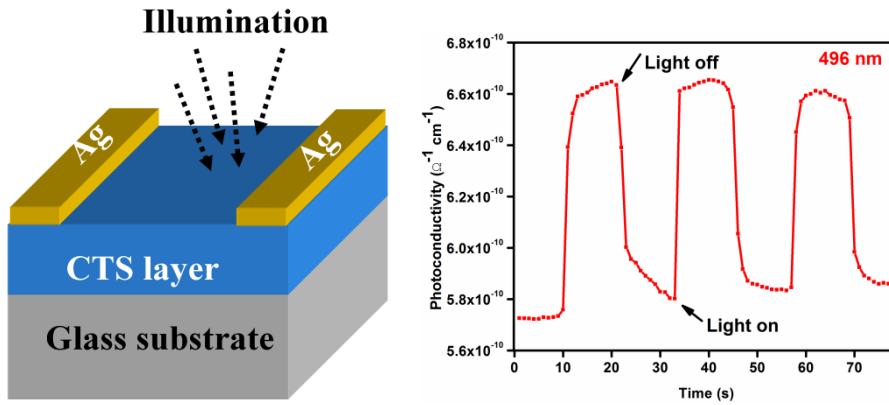


Fig. 9. (a) Schematic structure of visible light photodetector (b) photoconductivity verses time of the photodetector.

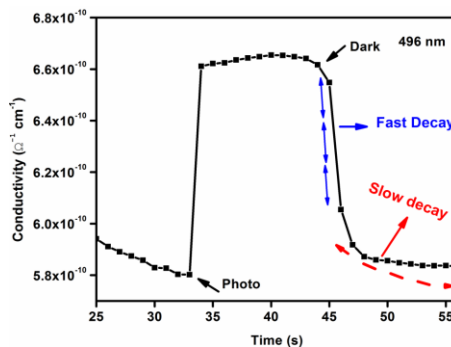


Fig. 10. The variation in photoconductivity as a function of time.

4. Conclusions

Co-evaporated Cu_2SnS_3 thin films were deposited at a constant substrate temperature of 250°C at different film thicknesses 285-910 nm. The impact of film thickness on physical properties of Cu_2SnS_3 films was reported. The XRD studies confirmed all the films exhibit tetragonal structure with dominated orientation along (112) direction. Raman analysis confirmed the presence of ternary phase (Cu_2SnS_3) along with binary phases.

The morphological study shows that the distribution of granular shaped crystallites as function of thickness. AFM studies revealed that the variation in the surface roughness and particle size of the films with thickness. A tunable band gap can be observed for the Cu_2SnS_3 with film thickness. The as-deposited films are p-type nature and resistivity decreased from 10^{-2} to 10^{-3} with film thickness 285 nm to 910 nm. Photodetectors are fabricated and characterized. The devices exhibited time dependent stability in photocurrent response for different ON/OFF cycles. The surface and bulk carrier life time of the device reported.

References

- [1] S. Fiechter, M. Martinez, G. Schmidt, W. Henrion, Y. Tamm, *Journal of Physics and chemistry of Solids* 64, 1859 (2003).
- [2] P. A Fernandes, P. M. P. Salome, A. F. Da Cunha, *Journal of Physics D: Applied Physics* 43, 215403 (2010).
- [3] H. Dahman, S. Rabaoui, A. Alyamani, L. El Mir, *Vacuum* 101, 208 (2014).
- [4] M. Onoda, X. Chen, A. Sato, H. Wada, *Materials Research Bulletin* 35, 1563 (2000).
- [5] J. Han, Y. Zhou, Y. Tian, Z. Huang, X. Wang, J. Zhong, Z. Xia, B. Yang, H. Song, J. Tang, *Frontiers of Optoelectronics* 7, 37 (2014).
- [6] V. Robles, T. F. Trigo, C. Guillén, J. Herrero, *Thin Solid Films* 582, 249 (2015).
- [7] U. Chalapathi, Y. Jayasree, S. Uthanna, V. S. Raja *Vacuum* 117, 121 (2015).
- [8] I. Y. Kim, J. Y. Lee, U. V. Ghorpade, M. P. Suryawanshi, D. S. Lee, J. H. Kim, *Journal of Alloys and Compounds* 688, 12 (2016).
- [9] P. Zhao, S. Cheng, *Advances in Materials Science and Engineering* 2013, 1 (2013).
- [10] R. Bodeux, J. Leguay, S. Delbos, *Thin Solid Films* 582, 229 (2015).
- [11] K. Chino, J. Koike, S. Eguchi, H. Araki, R. Nakamura, K. Jimbo, H. Katagiri, *Japanese Journal of Applied Physics* 51, 10NC35 (2012).
- [12] N. Aihara, A. Kanai, K. Kimura, M. Yamada, K. Toyonaga, H. Araki, A. Takeuchi, H. Katagiri, *Japanese Journal of Applied Physics* 53, 05FW13 (2014).
- [13] S. A. Vanalakar, G. L. Agawane, A. S. Kamble, C. W. Hong, P.S. Patil, J. H. Kim, *Solar Energy Materials and Solar Cells* 138, 1(2015).
- [14] S. Kahramana, S. Çetinkaya, S. Yaşar, I. Bilicanc, *Philosophical Magazine* 94, 3149 (2014).
- [15] M. Adelifard, M. M. B. Mohagheghi, H. Eshghi, *Physica Scripta* 85, 035603 (2012).
- [16] M. Bouaziz, M. Amlouk, S. Belgacem, *Thin Solid Films* 517, 2527(2009).
- [17] U. Chalapathi, Y. Jayasree, S. Uthanna, V. S. Raja, *Physical Status Solidi A* 210 No. 11, 2384 (2013).
- [18] Y. Tan, Z. Lin, W. Ren, W. Long, Y. Wang, X. Ouyang, *Materials Letters* 89, 240 (2012).
- [19] S. Rabaoui, H. Dahman, N. B. Mansour, L. E. Mir, *Journal of Materials Science: Materials in Electronics* 26, 1119 (2014).
- [20] H. Guan, H. Shen, C. Gao, X. He, *Journal of Materials Science: Materials in Electronics* 24, 1490 (2013).
- [21] Z. Su, K. Sun, Z. Han, F. Liu, Y. Lai, J. Li, Y. E. Liu, *Journal of Materials Chemistry* 22, 16346 (2012).
- [22] S. Kahraman, S. Çetinkaya, H. M. Çakmak, H. A. Çetinkara, H. S. Güder, *International Journal of Materials Research* 104, 1020 (2013).
- [23] T. S. Reddy, R. Amiruddin, M. C. Santhosh Kumar, *Solar Energy Materials and Solar Cells* 143, 128 (2015).

- [24] T. E. Manjulavalli, A. G. Kannan, *International Journal of ChemTech Research* 8(10), 259 (2015).
- [25] H. D. Shelke, A. C. Lokhande, V. S. Raut, A. M. Patil, J. H. Kim, C. D. Lokhande, *Journal of Materials Science: Materials in Electronics* 28, 79121(2017).
- [26] U. Chalapathi, B. Poornaprakash, S. H. Park, *Vacuum* 131, 22(2016).
- [27] P. A. Fernandes, P. M. P. Salome, A. F. D. Cunha, *Journal of Alloys and Compounds* 509, 7600 (2011).
- [28] T. S. Reddy, M. C. Santhosh Kumar, *Ceramics International* 42, 12262 (2016).
- [29] G. Barone, T. G. Hibbert, M. F. Mahon, K. C. Molloy, L. S. Price, I. P. Parkin, A. M. E. Hardy, M. N. Field, *Journal of Materials Chemistry* 11, 464 (2011).
- [30] M. R. R. Menon, S. Ranjbar, M. G. Sousa, P. A. Fernandes, A. F. D. Cunha, *Materials Research Express* 1, 045046 (2014).
- [31] H. Zhang, M. Xie, S. Zhang, Y. Xiang, *Journal of Alloys and Compounds* 602, 199 (2014).
- [32] A. I. Chih, Bessais B, *Superlattices and Microstructures* 97, 287(2016).
- [33] N. Revathi, P. Prathap, K.T. R. Reddy, *Solid State Electronics* 11, 1288 (2009).
- [34] M. M. A. Khan, W. Khan W, *Journal of Electronic Materials* 8, 4453(2016).
- [35] V. P. G. Vani, M. V. Reddy, K. T. R. Reddy, *ISRN Condensed Matter Physics* 2013, 1 (2013).
- [36] M. T. S. Nair, P. K. Nair, *Semiconductor Science and Technology* 6, 132(1991).
- [37] P. Prathap, N. Revathi, Y. P. V. Subbaiah, K. T. R. Reddy, *Journal of Physics: Condensed Matter* 20, 035205(2008).
- [38] J. Ji, Y. Ou, Z. Yua, Y. Yana, D. Wang, C. Yan, L. Liu, Y. Zhang, Y. Zhao, *Surface and Coatings Technology* 276, 587(2015).
- [39] Y. Gupta, P. Aruna, A. A Naudi, *Thin Solid Films* 612, 310 (2016).
- [40] P. Jain, P. Arun, *Thin Solid Films* 548, 241(2013)
- [41] F. D. Benedetto, I. Bencist, S. Caporali, *Progress in Photovoltaics: Research and Applications* 22, 97 (2014).
- [42] T.S. Reddy, M. C. S.Kumar, *RSC Advances* 6, 95680 (2016).
- [43] M. Banavoth, D. Sandra, S. B. Krupanidhi, *AIP Advances*, 3, 082132 (2013).
- [44] O. P.Singh, A. Sharma, K. S. Gour, *Solar Energy Materials and Solar Cells* 157, 28 (2016).
- [45] S. Dias, S. B. Krupanidhi, *AIP Advances* 6, 0252217 (2016).
- [46] R. Amiruddin, M. C. Santhosh Kumar, *Current Applied Physics* 16, 1052 (2016).
- [47] O. E. Shazlyya, A. A. M. Farag, M. A. Abdel Rafead, *Sensors and Actuators A* 239, 220 (2016).
- [48] F. Jiang, H. Shen, Z. J. Jiao, *ECS Journal of Solid State Science and Technology* 2 (11), 478 (2013).
- [49] M. C. Santhosh Kumar, B. Pradeep, *Vacuum* 72, 369 (2004).